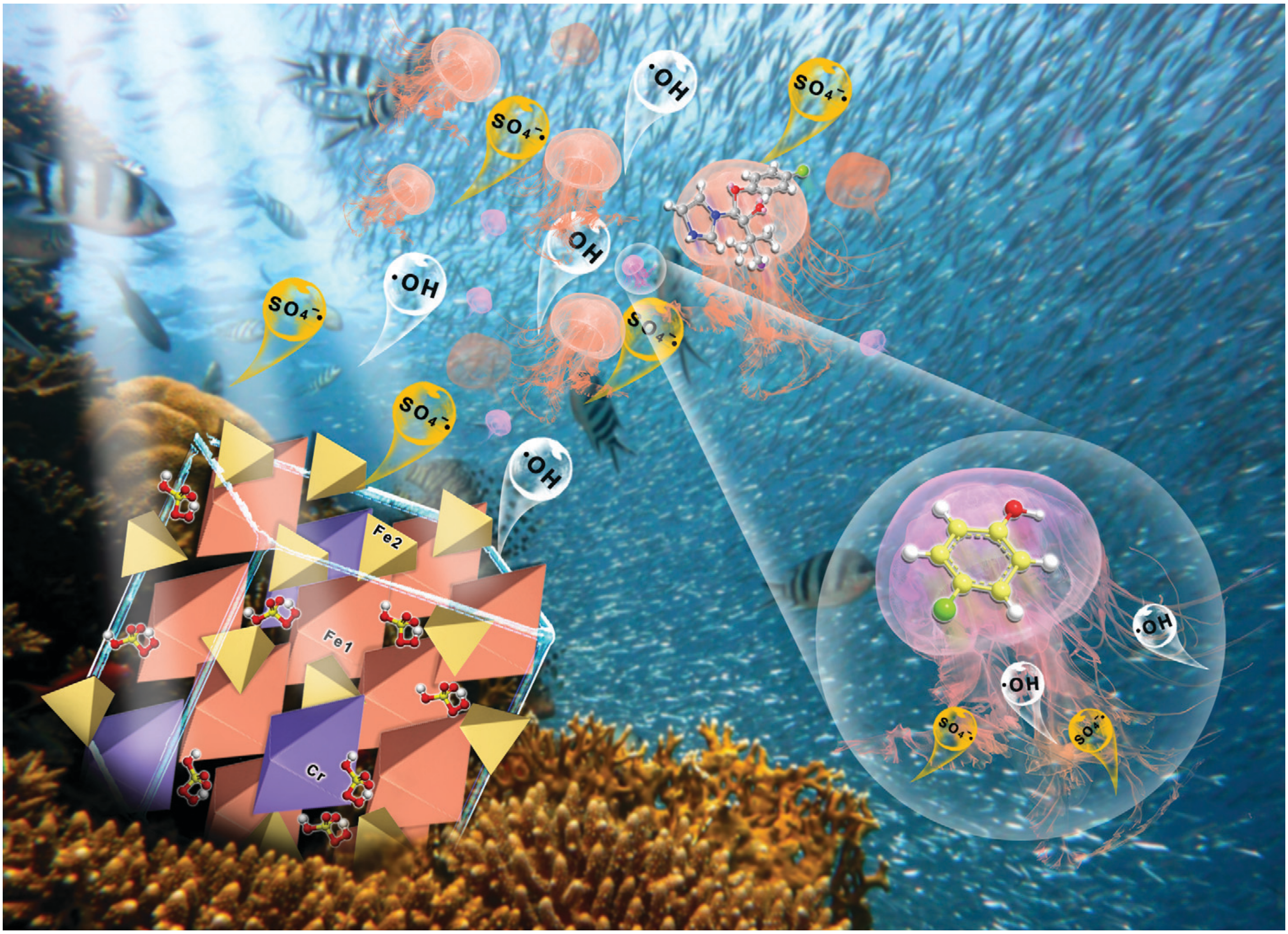

Featuring work from Dr. Yuanhong Zhong and Prof. Lin Yu at School of Chemical Engineering and Light Industry, Guangdong University of Technology, Guangzhou, China, and Dr. Zhi-Feng Chen at School of Environmental Science and Engineering, Guangdong University of Technology, Guangzhou, China.

Photocatalytic transformation of climbazole and 4-chlorophenol formation using a floral array of chromium-substituted magnetite nanoparticles activated with peroxymonosulfate

The results of this study have implications for environmental remediation in terms of the broad prospects for the UV/Cr-magnetite/PMS technique with excellent removal efficiency, good reusability of environmentally-friendly Cr-magnetite, and a decrease in the risks from highly toxic emerging contaminants due to lower toxicity intermediates.

As featured in:

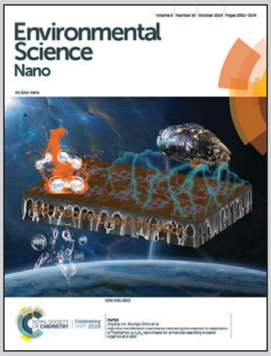

Environmental
Science
Nano

See Zhi-Feng Chen, Lin Yu *et al.*, *Environ. Sci.: Nano*, 2019, **6**, 2986.

ROYAL SOCIETY OF CHEMISTRY | Celebrating IYPT 2019

rsc.li/es-nano

Registered charity number: 207890

Environmental
Science
Nano

PAPER

View Article Online
View Journal | View Issue

Check for updates

Cite this: *Environ. Sci.: Nano*, 2019, **6**, 2986

Photocatalytic transformation of climbazole and 4-chlorophenol formation using a floral array of chromium-substituted magnetite nanoparticles activated with peroxymonosulfate†

Yuanhong Zhong,[a] Zhi-Feng Chen,‡*[b] Shi-Chao Yan,[b] Wen-Wen Wei,[b] Qianxin Zhang,[b] Guoguang Liu,[b] Zongwei Cai[bc] and Lin Yu‡*[a]

Received 18th June 2019,
Accepted 20th August 2019

DOI: 10.1039/c9en00673g

rsc.li/es-nano

Climbazole (CBZ) is an emerging contaminant with adverse effects on aquatic organisms. In this study, a floral array of chromium-substituted magnetite nanoparticles was synthesized, characterized, and used in photocatalytic degradation of CBZ. The results showed that Cr incorporation did not change the spinel structure of magnetite, but resulted in the obvious decrease of its crystallinity. The Cr content greatly influenced the morphology and micro-structure of magnetite nanoparticles, which led to a significantly larger surface area, and more abundant pores and surface hydroxyl groups. Factors such as the UV light source, catalyst concentration, initial level of CBZ, solution pH, peroxymonosulfate (PMS) dosage, and Cr level in magnetite affected the transformation of CBZ. Under the optimized photocatalytic conditions, *i.e.*, 0.2 g L^{-1} $Fe_{2.52}Cr_{0.48}O_4$, 2.0 μmol L^{-1} CBZ, 1.0 mmol L^{-1} PMS, and pH = 3.08, CBZ was almost completely eliminated within 30 min, which was much faster than under photodegradation, biodegradation, or chlorination reported previously. The reactive oxygen species including $^{\bullet}OH$ and $SO_4^{\bullet-}$ coexisted and participated in the photocatalytic reaction. The GC-MS analysis revealed the generation of 4-chlorophenol (4-CP) as a primary intermediate following CBZ transformation, based on the stoichiometric relationship between CBZ and 4-CP. The resultant 4-CP in the present study does not increase the risk to aquatic life. The results highlight an environmentally friendly strategy for effective elimination of CBZ.

Environmental significance

Climbazole (CBZ) is a common imidazole fungicide with a chlorophenol residue. The presence of climbazole in the aquatic environment will pose potential risks to aquatic organisms. The primary intermediate 4-chlorophenol (4-CP) is a toxic contaminant that affects aquatic life and is ranked high among the pollutants listed by the US Environmental Protection Agency and the European Union. However, the production of chlorophenol during the removal of organic chemicals was often ignored in previous reports. Therefore, the photocatalytic transformation of CBZ and 4-CP formation using a floral array of chromium-substituted magnetite nanoparticles activated with peroxymonosulfate were investigated. With the advantage of unique microtopography and microstructure, the chromium-substituted nano-magnetite displayed a significant activity in CBZ transformation, and the removal efficiency of CBZ was at least four-fold higher than that of photodegradation, biodegradation, or chlorination reported by other studies. Furthermore, the resultant 4-CP in the present study does not increase the risks to aquatic organisms. Our results provide an environmentally friendly strategy for effective elimination of CBZ and minimization of toxic by-product formation.

1. Introduction

Climbazole is a common imidazole fungicide with a chlorophenol residue. It is extensively used as an active antifungal ingredient in personal care products such as shampoos, hair lotions, face creams, and foot-care products. In April 2017, the Scientific Committee on Consumer Safety (SCCS) indicated a maximum concentration of 0.5% in leave-on products when climbazole was applied as a cosmetic preservative. The committee also proposed to lower the maximum concentration of climbazole to 0.2% with the

---

[a] School of Chemical Engineering and Light Industry, Guangdong University of Technology, Guangzhou 510006, China. E-mail: gych@gdut.edu.cn
[b] Guangzhou Key Laboratory of Environmental Catalysis and Pollution Control, Guangdong Key Laboratory of Environmental Catalysis and Health Risk Control, School of Environmental Science and Engineering, Institute of Environmental Health and Pollution Control, Guangdong University of Technology, Guangzhou 510006, China. E-mail: chenzhf@gdut.edu.cn
[c] State Key Laboratory of Environmental and Biological Analysis, Department of Chemistry, Hong Kong Baptist University, Hong Kong, SAR, China

† Electronic supplementary information (ESI) available: Additional Text A.1–A.6, Tables S1 and S2 and complementary Fig. S1–S5. See DOI: 10.1039/c9en00673g

‡ Present address: No.100 Waihuan Xi Road, Guangzhou Higher Education Mega Center, Panyu District, Guangzhou 510 006, China.

exception of cosmetics used on a full body area.[1,2] The usage of climbazole was estimated to be 345 tons annually in China,[3] while it ranged from 100 tons to 1000 tons in the European Union.[4] After application, climbazole is flushed into treatment plants along with wastewater. However, the rates of aqueous removal of climbazole were reported to range from 34% to 76%,[3,5,6] indicating incomplete elimination in wastewater treatment plants. Climbazole accumulates in the aquatic environment with potentially adverse effects on aquatic organisms. Richter *et al.*[7] demonstrated that climbazole is acutely toxic to water lentil *Lemna minor* with a median effective concentration of 19.0–33.9 μg L^{-1} based on the growth rate or biomass. According to a previous report, this chemical posed medium risks to aquatic organisms.[5] Therefore, it is necessary to regulate the discharge of climbazole into the aquatic environment.

Azole fungicides are recalcitrant to biodegradation.[8–10] The biodegradation rate of climbazole by freshwater microalga *Scenedesmus obliquus* was quite slow, with half-lives of 4.41–5.20 days.[11] In addition to biodegradation, chlorination and photodegradation were used for the elimination of climbazole.[12] The chlorine oxidation of climbazole was very poor, with a half-life of 30 h. In UV photolysis, when the reaction time was up to 60 min, climbazole was almost completely eliminated under irradiation with a 10 W low-pressure mercury lamp (λ = 254 nm). Treatment with a 250 W high-pressure mercury lamp (λ = 254–425 nm) improved the degradation rate of climbazole. It is not practical to use a 250 W lamp for the photolysis of organic chemicals due to the higher costs entailed. Previous studies also reported a few by-products of degradation, which were generated *via* reductive/hydroxylative dechlorination and cleavage of the ether bond.[12,13] The by-product 4-chlorophenol (4-CP) was identified during the photolysis of climbazole.[13] Chlorophenols are toxic contaminants that affect the life of aquatic organisms and therefore ranked high among the pollutants listed by the US Environmental Protection Agency[14] and the European Union (EU).[15,16] However, the minor by-products of molecular degradation such as chlorophenols were often ignored.

In recent years, nanoparticle-mediated heterogeneous photocatalytic degradation has been considered as a promising technique for the removal of environmental pollutants.[17–19] Magnetite (Fe_3O_4) is an ideal catalyst for practical application in controlling environmental pollution because of its strong photocatalytic activities based on redox cycling of Fe(II) and Fe(III),[17,20] which mediate the enzymatic catalysis of H_2O_2 generating $^{\bullet}OH$ *via* heterogeneous Fenton technology. Furthermore, it is a magnetic compound, which can be easily separated from the reaction solution using a magnet, indicating excellent environmental compatibility. Therefore, the usage of magnetite as a Fenton-like catalyst for the degradation of organic pollutants in water has received a great deal of attention. With a structure similar to that of H_2O_2, the oxidants peroxymonosulfate (PMS) and persulfate utilize the O–O bonds instead of H_2O_2.[21] One or both hydrogen atoms in H_2O_2 can be replaced by SO_3 to generate HSO_5^- and $S_2O_8^{2-}$, respectively. By contrast, PMS and PS promote stability and allow easy storage. Both oxidants can be activated to generate $SO_4^{\bullet -}$, which is a powerful radical that oxidizes most organic compounds in wastewater. Therefore, magnetite-activated PMS or PS is of interest as a very promising technique for the degradation of non-biodegradable contaminants. Bulk magnetite and magnetite substituted with cations (*e.g.*, Mn, Cr, and Ti) are found as minerals on the earth surface.[22] Ultraviolet A (UVA, λ = 315–400 nm) constitutes about 3% of sunlight, which penetrates the Earth's atmosphere and reaches the ground. As expected, climbazole undergoes transformation in the natural environment with cation-substituted magnetite and UVA irradiation. The introduction of PMS was reported to enhance the photocatalytic performance of nanoparticles.[22] Studies investigating cation-substituted, magnetite-induced heterogeneous photocatalytic degradation of climbazole under the combination of UVA and PMS have yet to be reported.

We previously reported the highest photocatalytic redox activities of Cr-substituted magnetite compared with other transition metal substitutions.[17] The effect of Cr incorporation on the Fenton catalytic activity of magnetite was the focus of the investigation, without elucidating the effect of Cr incorporation on the micromorphology, interfacial structure, or activation of PMS or PS. Therefore, this study was conducted to synthesize and characterize a floral chromium-substituted magnetite ($Fe_{3-x}Cr_xO_4$–F), to investigate the photocatalytic performance and mechanism of climbazole in a $Fe_{3-x}Cr_xO_4$–F/UVA/PMS system, and to evaluate the potential risk associated with the intermediate product 4-CP. The results suggest an effective strategy for the removal of climbazole and elucidate the fate of climbazole in the aquatic environment. Additionally, the new insights into the effect of Cr cation substitution on the micromorphology and interfacial activity of nano-magnetite are of vital importance for the industrial application of Cr-magnetite.

2. Experimental procedure

2.1. Chemicals and reagents

All chemicals and reagents employed in this study were of analytical grade and derived from commercial sources and used without further purification. The commercial nano-magnetite was obtained from Shanghai Macklin Biochemical Co., Ltd (China). PMS ($KHSO_5 \cdot 0.5KHSO_4 \cdot 0.5K_2SO_4$, ≥47% $KHSO_5$) was purchased from Aladdin Chemicals. Climbazole (CBZ, 99.9%) and 4-chlorophenol (4-CP) were supplied by Dr. Ehrenstorfer from Germany and AccuStandard from USA, respectively. *N*,*O*-Bis(trimethylsilyl) trifluoroacetamide (BSTFA) was purchased from Regis Chemical Company (USA). Oasis HLB cartridges (500 mg, 6 mL) were obtained from Waters Corporation (Milford, MA, USA). Methanol of HPLC grade was purchased from Merck. Stock solutions of CBZ (2 mmol L^{-1}) and 4-CP (1.00 g L^{-1}) were prepared in methanol and stored at −20 °C.

2.2. Preparation of floral Cr-magnetite samples

Floral Cr-magnetite samples ($Fe_{3-x}Cr_xO_4$–F, $0 \le x \le 1$) were synthesized using an adjusted microwave-assisted technique as reported in our previous nanomagnetite synthesis. The detailed mechanisms are described in Text A.1 in the ESI.† The samples were denoted as $Fe_{3-x}Cr_xO_4$ ($0 < x < 1$). The catalytic activities were compared by preparing pure nano-magnetite samples using a similar procedure without $CrCl_3·6H_2O$, and the commercial products Fe_3O_4 and Fe_3O_4–C were also obtained.

2.3. Characterization of Cr-magnetite samples

The contents of Fe and Cr in the synthetic samples were determined using a Thermo Scientific iCAP-6000 inductively coupled plasma atomic emission spectrometer (ICP-AES). The obtained samples were characterized by powder X-ray diffraction (PXRD), BET specific surface area, distribution of pore size, scanning electron microscopy (SEM), transmission electron microscopy (TEM), Raman spectroscopy, and X-ray photoelectron spectroscopy (XPS). The details of characterization are provided in Text A.2 in the ESI.†

2.4. Heterogeneous catalytic activity

The heterogeneous catalytic activities of the as-prepared samples were evaluated by monitoring the degradation of climbazole in water under UVA irradiation. The tests were carried out in a home-made photo-reactor. A hand-held torch was used as a UVA light source for the irradiation reaction, consisting of three 3 W LED light bulbs (λ = 365 nm). All batch kinetic experiments were performed in a 100 mL transparent double-beaker filled with circulating water. In order to avoid extraneous illumination, the beaker and UVA torch were wrapped in aluminium foil. Typically, 80 μL of CBZ stock solution (2 mmol L^{-1}) was poured into the beaker, and the solvent methanol was evaporated with a gentle stream of N_2 at room temperature. Thereafter, 80 mL of deionized water was used to re-dissolve the CBZ residue completely at a concentration of 2 μmol L^{-1} followed by the addition of 0.016 g of catalyst to the solution. The reaction was initiated *via* simultaneous addition of PMS and turning on a UVA lamp. The pH of the solution following the addition of PMS was 3.0 ± 0.5. At specific intervals, aliquots of 1.0 mL reaction solution were withdrawn and mixed with 100 μL of 0.5 mol L^{-1} $Na_2S_2O_3$ immediately to quench the reaction. Using a magnet to remove the catalyst, the supernatant was transferred into a 2 mL vial before analysis. The concentrations of CBZ were analyzed with a Waters e2695 high-performance liquid chromatograph (HPLC) connected to a diode array detector (DAD). The detailed instrumental conditions are described in Text A.3 of the ESI.† The limits of detection and quantitation of CBZ were 0.02 μmol L^{-1} and 0.07 μmol L^{-1}, respectively.

For the identification of 4-CP or other potential intermediates, another set of experiments was conducted with a higher volume of 100 mL solution. The initial concentration (2 μmol L^{-1}) of CBZ was in accordance with that of the kinetic experiments. Each 100 mL reaction solution with reaction times of 0 (blank control), 10 min, 20 min, and 40 min was transferred into an amber bottle followed by the addition of $Na_2S_2O_3$ to quench the reactions. The potential intermediates were extracted from the solution samples *via* solid phase extraction. For GC-MS analysis, the extracts were treated appropriately before sample injection. For LC-HRMS analysis, the extracts were directly injected into an LC system and analyzed by HRMS. The detailed procedures of solid phase extraction and pre-column derivation are indicated in Text A.4 in the ESI.† GC-MS analysis was carried out on a Thermo TRACE™ 1300 gas chromatograph connected to a TSQ 8000 Evo mass spectrometer (Thermo Scientific, USA) with an electronic ionization (EI) source. UHPLC-HRMS was performed using a Dionex Ultimate 3000 ultra-high-performance liquid chromatograph (UHPLC) coupled to a Thermo Scientific Q Extractive Focus mass spectrometer (Thermo Scientific, USA). The instrumental operating parameters of GC-MS and UHPLC-HRMS are indicated in Text A.5 and Table S1 in the ESI.† The limits of detection and quantitation of 4-CP were 2.75×10^{-5} μmol L^{-1} and 8.34×10^{-5} μmol L^{-1}, respectively.

Two reference experiments were also performed: (i) with light irradiation in the absence of a catalyst (with H_2O_2 only) and (ii) without a catalyst and H_2O_2 (blank). Hydroxyl radicals ($^{\bullet}OH$) and sulfate radicals ($SO_4^{\bullet-}$) generated during the photocatalytic degradation were estimated by electron spin resonance (ESR) using dimethyl pyridine *N*-oxide (DMPO) as a capture agent.

2.5. Risk assessment of 4-CP

A preliminary risk assessment was performed using the risk quotient (RQ) approach based on the European Commission Technical Guidance Document.[23] The RQ value was calculated by dividing the measured environmental concentration (MEC) value by the predicted no-effect concentration (PNEC) value (eqn (1)). The values of RQ < 0.1, 0.1 ≤ RQ < 1, and RQ ≥ 1 indicated minimal, medium, and high risks, respectively.[24] Based on the toxicity of a chemical, the calculation of PNEC was derived by an assessment factor approach or a species sensitivity distribution curve. The detailed description is provided in Text A.6 in the ESI.†

$$RQ = MEC/PNEC. \tag{1}$$

3. Results and discussion

3.1. XRD patterns

Based on the chemical analysis (Table 1), the chemical formulae of the synthetic samples were determined as Fe_3O_4, $Fe_{2.76}Cr_{0.24}O_4$, $Fe_{2.52}Cr_{0.48}O_4$, and $Fe_{2.28}Cr_{0.72}O_4$. Notably, the Cr contents of all the samples with the formula $Fe_{3-x}Cr_xO_4$ were close to the added quantity, and the Fe content decreased after the incorporation of Cr, indicating the replacement of Fe with Cr metal in the magnetite structure. Fig. 1A illustrates the XRD patterns of the synthetic $Fe_{3-x}Cr_xO_4$ samples, and all the samples showed spinel structures corresponding to the standard cards of magnetite (JCPDS: 19-

Table 1 Chemical analysis of the samples $Fe_{3-x}Cr_xO_4$ ($0 \leq x \leq 1$)

Sample	Addition of Fe : Cr	C_{Cr}/mg L^{-1}	C_{Fe}/mg L^{-1}	x	Chemical formulae
1	Commercial	0.19	731.90	0.00	Fe_3O_4–C
2	3.0 : 0.0	0.02	709.29	0.00	Fe_3O_4
3	2.75 : 0.25	50.39	635.35	0.24	$Fe_{2.76}Cr_{0.24}O_4$
4	2.50 : 0.50	100.63	571.34	0.48	$Fe_{2.52}Cr_{0.48}O_4$
5	2.25 : 0.75	143.49	487.12	0.72	$Fe_{2.28}Cr_{0.72}O_4$

0629) and chromite (JCPDS: 34-0140). Thus, the introduction of Cr did not change the inverse-spinel structure. By contrast, the peaks of the Cr-substituted magnetite samples were broadened and weakened with a decreased intensity, revealing the poor crystallinity of the three samples and reduced size of the crystallites compared with that of Fe_3O_4. The shift of peaks at *ca.* 35.5° toward a lower diffraction angle (inset in Fig. 1A) indicated the incorporation of Cr into the inverse spinel structure, which resulted from the slightly smaller ion radius of Cr^{3+} (0.63 Å) compared with that of Fe^{3+} (0.65 Å). Accordingly, a slight increase in lattice parameter a_0 was observed (Table 2). In spite of the same valence state and isostructural oxides between Cr^{3+} and Fe^{3+}, Cr substitution resulted in the distortion of the FeO_6 octahedron and the increase of OH and H_2O contents in the magnetite structure (according to XPS results), due to their different ionic radii, which caused lattice strain and deviated from the ideal Vegard relationship.[25] This can also be interpreted simply as a reduced growth of the magnetite crystal in the *z*-direction in the presence of Cr, which affects the morphology of Cr-magnetite. Many analogous cases were reported elsewhere for aluminium substituted on hematite.[25–27]

3.2. Micro-structure and micro-morphology of magnetite

Fig. 1B shows the SEM images of the commercial Fe_3O_4–C and synthetic $Fe_{3-x}Cr_xO_4$ samples. Fe_3O_4–C exhibited mainly spherical morphologies (Fig. 1B1) with an average size of approximately 180 nm ($n \approx 50$ particles). The synthetic Fe_3O_4 nanoparticles showed good dispersion and rod-like shape measuring 12–36 nm laterally and 45–156 nm longitudinally (Fig. 1B2). After incorporating Cr, the micromorphology of magnetite displayed significant changes (Fig. 1B3–B5). The sample $Fe_{2.76}Cr_{0.24}O_4$ assembled into multilayered porous structures with interconnected nano-flakes, as shown in the HRTEM images (Fig. S1†). The thickness of nano-flakes was approximately 8–16 nm. With the increased Cr content, no nano-flakes were detected in $Fe_{2.52}Cr_{0.48}O_4$ and $Fe_{2.28}Cr_{0.72}O_4$ samples. Instead, a floral assembly of nanorod clusters of layered flowers was observed. This phenomenon suggested that the isomorphous replacement of Cr greatly influenced the morphology and micro-structure of magnetite. The change in surface energy of magnetite crystals resulting from Cr replacement led to a minor distortion in the crystal structure and even altered the preferred growth orientation of the crystal.

As shown in Table 2, the BET surface areas of the synthetic magnetite samples were substantially larger than that of the commercial samples (9.2 m^2 g^{-1}). The Cr substitutions in magnetite apparently enhanced its specific surface area in direct proportion to the increased Cr content. The sample $Fe_{2.28}Cr_{0.72}O_4$ exhibited the highest surface area (184.4 m^2 g^{-1}), which was nearly 20-fold greater than that of Fe_3O_4–C and five-fold higher than that of the synthetic Fe_3O_4. This result suggested that the Cr replacement may lead to the formation of microporous or mesoporous magnetite. Fig. 1C illustrates the N_2 adsorption–desorption isotherms of the samples. According to the classification of the International Union of Pure and Applied Chemistry (IUPAC), these adsorption–desorption isotherms of the synthetic samples represented the type IV category,[28,29] and the hysteresis loops were assigned to the type H3 profile, which was associated with aggregates of plate-like particles or slit-shaped pores.[30] Also, it suggested a mesoporous structure.[31,32] Fig. 1D shows the pore size distribution in the adsorption branch (BJH model) of the $Fe_{3-x}Cr_xO_4$ samples. Almost no pore structure was found in Fe_3O_4–C and the synthetic Fe_3O_4 samples. A significant pore distribution occurred with the incorporation of Cr. With the increased Cr content, both the micropore volume (<2 nm) and mesopore volume (2–50 nm) were increased, whereas the average pore sizes were reduced (Table 2).

3.3. XPS and Raman spectra

XPS based on the specific binding energy was used to investigate the surface element composition and valence state. The Fe 2p XPS spectra (Fig. 2A) of the Fe_3O_4–C and $Fe_{3-x}Cr_xO_4$ NPs show a characteristic doublet located at 709.8–710.9 eV and 723.0–724.8 eV, which corresponds to Fe $2p_{3/2}$ and Fe $2p_{1/2}$, respectively.[33] The fitted parameters are displayed in Table 3. As for Fe_3O_4–C, the fitting Fe $2p_{3/2}$ (Fe $2p_{1/2}$) binding energy was 710.3 eV (723.6 eV) for Fe^{II} and 711.5 eV (725.1 eV) for Fe^{III}. The small satellite peak around 718.5 eV (peak 5) was attributed to the air-oxidized surface of Fe_3O_4 to γ-Fe_2O_3 during sample storage or XPS preparation. The binding energies of Fe $2p_{3/2}$ and Fe $2p_{1/2}$ of the synthetic Fe_3O_4 slightly deviated from those of Fe_3O_4–C, which was consistent with our previously reported spectra of rod-like magnetite particles.[34] However, the characteristic doublet (Fe $2p_{3/2}$ and Fe $2p_{1/2}$) of Cr-substituted magnetite slightly shifted to higher energies, indicating that the substitution of Cr altered the local environment of Fe atoms. Their binding energies for Fe $2p_{3/2}$ and Fe $2p_{1/2}$ (Table 3) were very close to the Fe 2p (725 eV for Fe $2p_{1/2}$ and 710.6 eV for Fe $2p_{3/2}$) of Fe_2CrO_4 in the National Institute of Standards and Technology (NIST) XPS Standard Reference Database 20 (Version 4.1), indirectly suggesting the entry of Cr cations into the magnetite structure. The Cr 2p spectra (Fig. 2C) of $Fe_{3-x}Cr_xO_4$ ($x > 0$) nanoparticles showed a characteristic doublet (Cr $2p_{3/2}$ and Cr $2p_{1/2}$) located at 577.0–576.8 eV and 586.9–586.6 eV, respectively. Furthermore, it was identical to the reported standard Cr 2p of α-Cr_2O_3,[35] suggesting that Cr

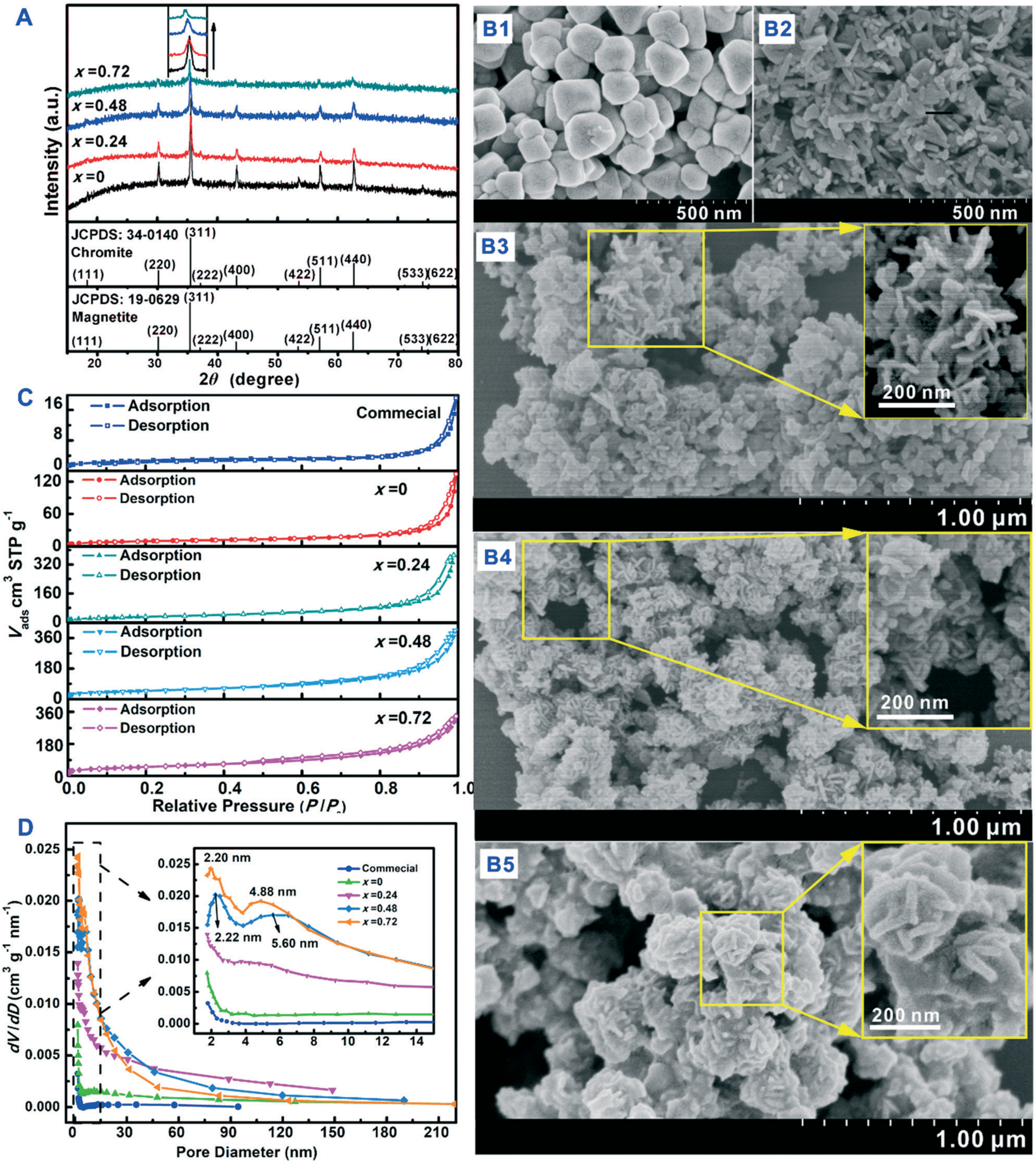

Fig. 1 A: XRD patterns of the synthetic $Fe_{3-x}Cr_xO_4$ samples; B: SEM images of the commercial Fe_3O_4–C and synthetic $Fe_{3-x}Cr_xO_4$ samples, (B1): Fe_3O_4–C, (B2): Fe_3O_4, (B3): $Fe_{2.76}Cr_{0.24}O_4$, (B4): $Fe_{2.52}Cr_{0.48}O_4$, and (B5): $Fe_{2.28}Cr_{0.72}O_4$; C: the N_2 adsorption–desorption isotherms of the samples; D: pore size distribution in the adsorption branch (BJH model) of the $Fe_{3-x}Cr_xO_4$ samples, inset: enlarged scale.

in the $Fe_{3-x}Cr_xO_4$ structure existed in the Cr^{3+} form. The recorded O 1s spectra (Fig. 2B) of Fe_3O_4–C and Fe_3O_4 were resolved into two main peaks at approximately 529.8 eV and 531.0 eV, respectively, which were attributed to the lattice oxygen (Fe–O) and adsorbed oxygen or surface hydroxyl species (–OH),[36] respectively. After Cr substitution, the peak intensities of surface hydroxyl species were enhanced, which was consistent with our previous results related to the thermal analysis of Cr-substituted magnetite.[37] For $Fe_{3-x}Cr_xO_4$ samples, an additional peak at a higher binding energy around 532.1 eV was assigned to the surface-adsorbed water.[38]

Table 2 Lattice parameters, BET surface areas, and particle sizes of the $Fe_{3-x}Cr_xO_4(0 \le x \le 1)$ samples

Sample	a_0/Å	BET/$m^2\ g^{-1}$	Mean pore size/nm
Fe_3O_4–C	8.380	9.2	—
Fe_3O_4	8.373	36.0	27.4
$Fe_{2.76}Cr_{0.24}O_4$	8.374	118.1	19.3
$Fe_{2.52}Cr_{0.48}O_4$	8.382	175.7	14.2
$Fe_{2.28}Cr_{0.72}O_4$	8.393	184.4	11.3

Further critical details of the chemical composition and homogeneity of the samples were identified by laser Raman spectroscopy. The Raman spectra of the $Fe_{3-x}Cr_xO_4$ samples (Fig. 2D) show two Raman bands located at about 668 cm^{-1} and 543 cm^{-1}, which were assigned to the A_{1g} and T_{2g} modes of magnetite, respectively. The results corresponded to those of earlier Raman studies involving synthetic magnetite. No additional characteristic bands for maghemite (720 cm^{-1}, 500 cm^{-1}, and 350 cm^{-1}), hematite (390 cm^{-1}, 280 cm^{-1}, and 220 cm^{-1}), or goethite (1110 cm^{-1} and 880 cm^{-1}) were detected,[39–41] suggesting that the synthetic $Fe_{3-x}Cr_xO_4$ was a pure magnetite, consistent with XRD results. Notably, the substitution of Cr for Fe in the structure reduced the intensity of the Raman peak at *ca.* 673 cm^{-1} and expanded its width. Meanwhile, the peak at *ca.* 547 cm^{-1} increased with the increased Cr content.

3.4. Degradation of climbazole by $Fe_{3-x}Cr_xO_4$-activated PMS

We analyzed the effect of various reaction parameters on the catalytic performance of $Fe_{3-x}Cr_xO_4$ by activation of PMS. Considering $Fe_{2.52}Cr_{0.48}O_4$ as an example, the factors influencing the degradation were studied. As shown in Fig. 3a, less than 5% of CBZ could be removed through adsorption by $Fe_{2.52}Cr_{0.48}O_4$. Almost no degradation of CBZ was observed after 40 min of reaction with only PMS or $Fe_{2.52}Cr_{0.48}O_4$ under UV irradiation. Under natural light conditions, the CBZ in the PMS/$Fe_{2.52}Cr_{0.48}O_4$ system was degraded by about 25% after 40 min. The low removal rate was attributed to the reduced catalytic activity of Fe^{III} compared with that of Fe^{II} and the lack of effective reduction of the generated Fe^{III} on the $Fe_{2.52}Cr_{0.48}O_4$ surface to Fe^{II} under natural irradiation. Both phenomena resulted in insufficient $^{\bullet}OH$ radical generation. Following irradiation with UV light, the degradation efficiency of the $Fe_{2.52}Cr_{0.48}O_4$/UV system was greatly improved, and CBZ was almost completely degraded within 30 min, indicating that $Fe_{2.52}Cr_{0.48}O_4$ exhibited adequate catalytic activity with PMS activation under UV light (eqn (2)) due to successful reduction of Fe^{III} on the magnetite surface to Fe^{II} (eqn (3)) under UV light irradiation.[42] In addition, the UV/Fenton catalytic degradation of CBZ by $Fe_{2.52}Cr_{0.48}O_4$ nanoparticles was also conducted for comparison. But only 20% of CBZ can be eliminated after 40 min of reaction with 20 mmol L^{-1} H_2O_2.

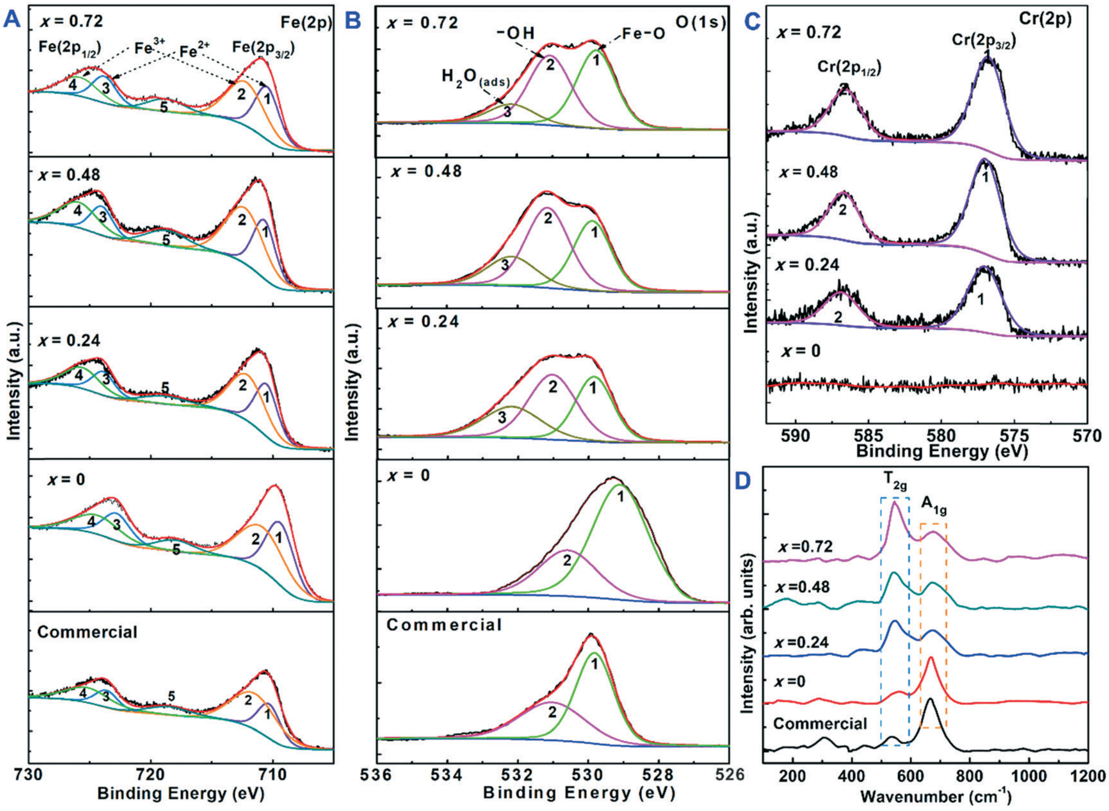

Fig. 2 Fitting results of the Fe 2p (A), Cr 2p (B), and O 1s (C) XPS spectra of the $Fe_{3-x}Cr_xO_4$ $(0 \le x \le 1)$ samples; Raman spectra of the $Fe_{3-x}Cr_xO_4$ samples (D).

Table 3 Peak fitting parameters of Fe 2p, Cr 2p, and O 1s spectra

	Peak center (eV)[a]									
	Fe					Cr		O		
Sample	1	2	3	4	5	1	2	1	2	3
Fe_3O_4–C	710.3	723.6	711.5	725.1	718.5	—	—	529.8	531.0	—
Fe_3O_4	709.4	722.8	710.9	724.4	718.0	—	—	529.9	531.2	—
$Fe_{2.76}Cr_{0.24}O_4$	710.5	723.9	712.1	725.9	718.8	577.0	586.9	529.8	531.0	532.1
$Fe_{2.52}Cr_{0.48}O_4$	710.7	724.0	712.3	725.9	718.7	576.9	586.7	529.9	531.1	532.2
$Fe_{2.28}Cr_{0.72}O_4$	710.5	723.8	712.2	725.8	718.7	576.8	586.6	529.8	531.1	532.2

[a] The value of %GL fixed to 20%.

Therefore, it is clear that the removal of CBZ by the $Fe_{2.52}Cr_{0.48}O_4$/UV/PMS system was more efficient than that by the $Fe_{2.52}Cr_{0.48}O_4$/UV/H_2O_2 system.

$$\equiv Fe^{II} + HSO_5^- \rightarrow \equiv Fe^{III} + SO_4^{\bullet-} + OH^- \quad (2)$$

$$\equiv Fe^{III} + h\nu \rightarrow \equiv Fe^{II} \quad (3)$$

The ionization constant pK_a of CBZ was 7.5,[7] suggesting that the removal of CBZ was probably affected by the pH of the solution. The results revealed that the pH value of the solution had a dramatic effect on the degradation efficiency of CBZ (Fig. 3b). In the system at pH 3.08, *i.e.*, without the addition of acid or lye, CBZ was almost completely degraded within 30 min. The removal rates of CBZ decreased sharply in the solution at pH $\leq$ 3.0 and pH $\geq$ 7. After reaction for 40 min, only about 30% of CBZ was degraded in the system at pH 9.01. The phenomenon was attributed to the addition of sulfuric acid leading to the inhibition of the activation of HSO_5^- to produce $SO_4^{\bullet-}$, and the addition of alkali neutralized a part of HSO_5^- and generated $SO_4^{\bullet-}$ in the system for further conversion to $^{\bullet}OH$ (eqn (4)).[43,44]

$$SO_4^{\bullet-} + OH^- \rightarrow SO_4^{2-} + {}^{\bullet}OH \quad (4)$$

The substantially lower lifetime of $^{\bullet}OH$ compared with that of $SO_4^{\bullet-}$ resulted in the reduction of the available PMS and consequently decreased the degradation efficiency of CBZ. Interestingly, this phenomenon differed from the reported results of UV photo-degradation of CBZ. Couteau *et al.*[45] demonstrated that the degradation efficiency of CBZ in the UV photo system was closely related to the solution pH, and the highest removal rate occurred at pH 9.0. However, Liu *et al.*[12] found that the initial pH of the solution had little effect on the degradation of CBZ in the UV system (λ = 254 nm). This discrepancy may be ascribed to the difference in reaction conditions. As we know, in the UV irradiation system, the removal of organic pollutants only depends on the UV photo-degradation. But in our study, the coexisting catalyst and PMS played a dominant role in CBZ degradation, which led to a completely different degradation process. In addition, the UV light source with a wavelength of 365 nm might also have some influence on the degradation of CBZ.

The effect of $Fe_{2.52}Cr_{0.48}O_4$ dosage ranging from 0 to 0.4 g L^{-1} on CBZ degradation was investigated. As shown in Fig. 3c, the proportion of CBZ degradation increased from 0 to 100% when the dosage of $Fe_{2.52}Cr_{0.48}O_4$ was increased from 0 to 0.2 g L^{-1}, indicating the high catalytic activity of $Fe_{2.52}Cr_{0.48}O_4$ in CBZ degradation. With the catalyst dosage increased to 0.3–0.4 g L^{-1}, the rate of catalytic degradation of CBZ by $Fe_{2.52}Cr_{0.48}O_4$ was not changed apparently. Compared with the control system, the addition of 0.25 mmol L^{-1} PMS resulted in an increased degradation of CBZ (Fig. 3d). With the PMS concentration rising to 1.00 mmol L^{-1}, the degradation efficiency of CBZ increased to 100% within 30 min, which may be attributed to PMS activation by Cr-magnetite and the produced $SO_4^{\bullet-}$ (eqn (1)), which is known to be a very strong single-electron oxidant. However, the CBZ degradation efficiency was decreased significantly under the dosage of PMS up to 1.50 mmol L^{-1}. The decline in the degradation of CBZ may be ascribed to the excessive $SO_4^{\bullet-}$ radicals quenching each other to form $S_2O_8^{2-}$ (eqn (5)) and the reaction with the redundant HSO_5^- to produce weaker $SO_5^{\bullet-}$ radicals (eqn (6)).[46]

$$SO_4^{\bullet-} + SO_4^{\bullet-} \rightarrow S_2O_8^{2-} \quad (5)$$

$$SO_4^{\bullet-} + HSO_5^- \rightarrow SO_5^{\bullet-} + HSO_4^- \quad (6)$$

Fig. 3e shows the effect of the initial CBZ concentration on the degradation mechanism. No obvious effect was seen in the degradation efficiency at a concentration of 1.0–2.0 μmol L^{-1}. The CBZ was almost completely degraded following a 30 min reaction. Nevertheless, when the concentration of CBZ was raised to 2.5 μmol L^{-1} (*i.e.*, 732.5 μg L^{-1}), the degradation rate declined to 81.5% after a reaction interval of 40 min, which may be due to the generation of $SO_4^{\bullet-}$ and $^{\bullet}OH$ radicals on the surface of the catalyst limited by the ratio of Fe^{III}/Fe^{II} on the magnetite surface, which restricted the amount of CBZ reacting with the radicals. The result suggested that the incremental initial CBZ concentration reduced the probability of the reaction between CBZ and radicals. Specifically, at a high concentration of CBZ, the reaction rate decreased relatively and lasted for a considerable duration. The degradation of CBZ catalyzed by Cr-magnetite with different levels of Cr

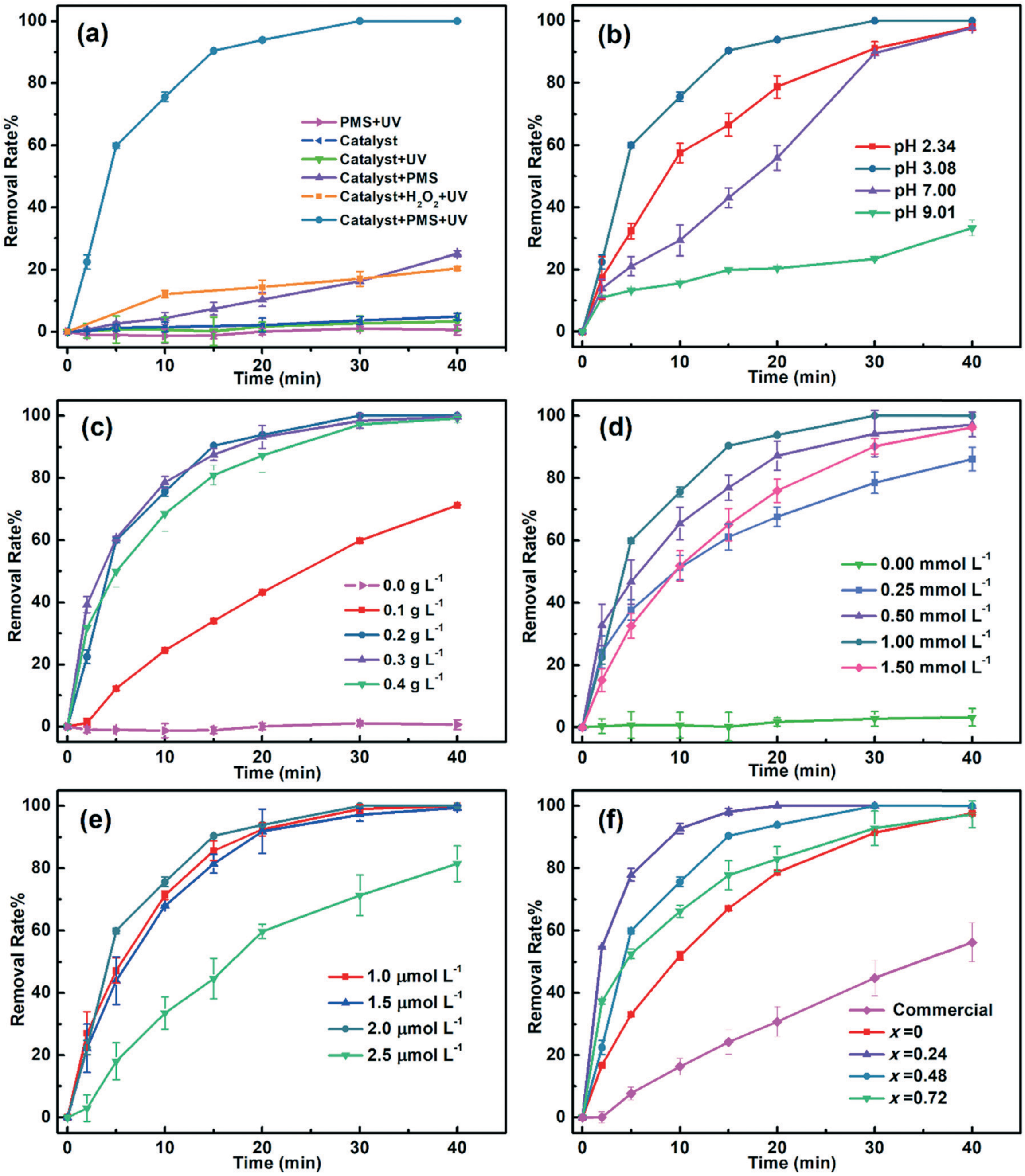

Fig. 3 Effect of various experimental conditions on the degradation of CBZ by activated PMS on Cr-magnetite: (a) UVA light source, (b) different initial pH values, (c) catalyst dosage, (d) PMS dosage, (e) different initial CBZ concentrations, and (f) Cr doping content (if not specified, the reaction conditions were: CBZ, 2.0 μmol L^{-1}; PMS, 1.0 mmol L^{-1}; H_2O_2: 20 mmol L^{-1}, $Fe_{2.52}Cr_{0.48}O_4$, 0.2 g L^{-1}; 80 mL; pH, 3.08; 25 °C).

content is shown in Fig. 3f. Under the test conditions, the elimination rate of CBZ in the Fe_3O_4–C system was about 55% after a 40 min reaction, compared with 97% in the synthetic Fe_3O_4 system. The catalytic activities of all the $Fe_{3-x}Cr_xO_4$ samples were stronger than those of pure magnetite, suggesting that Cr incorporation played an important role in enhancing the catalytic activity of magnetite in the UV/Fenton reaction. This may be attributed to the Cr ions participating in the activation process of PMS to generate $SO_4^{\bullet-}$ radicals which was thermodynamically favorable. The potential value of the redox pair Cr^{2+}/Cr^{3+} (0.408 V)[47] was lower than the standard redox potential (E^0) of PMS (1.82 V),[48] illustrating that it could initiate PMS activation similar to Fe^{2+}. Under UVA irradiation, the Cr^{III} on the Cr-magnetite surface could capture the photo-generated electrons (e^-) to form Cr^{II} (eqn (7)). Based on the redox potential, the generated $\equiv Cr^{II}$ had a high activity in activation of PMS as suggested in eqn (8).

$$\equiv Cr^{III} + e^- \rightarrow \equiv Cr^{II}, \quad E^0 = -0.408 \text{ V} \tag{7}$$

$$\equiv Cr^{II} + HSO_5^- \rightarrow \equiv Cr^{III} + SO_4^{\bullet-} + OH^-, \quad \Delta E = 2.228\ V \quad (8)$$

However, a slight decline occurred with the increased Cr content in $Fe_{3-x}Cr_xO_4$, which was contrary to a previous study analyzing Cr-magnetite using a heterogeneous Fenton catalyst, possibly due to the improvement in micropore volume of $Fe_{2.52}Cr_{0.48}O_4$ and $Fe_{2.28}Cr_{0.72}O_4$ samples following the incorporation of Cr. The micropore diameter ≤2 nm may not be conducive to the free entry and exit of the active component HSO_5^- of PMS, thus slowing down the degradation rate. Furthermore, with nanoflake morphology, the sample $Fe_{2.76}Cr_{0.24}O_4$ exposed more active facets. Our previous study demonstrated that the heterogeneous catalytic activities of Fe_3O_4 were morphology dependent, and the sample with nanoplate morphology showed a substantially stronger catalytic activity compared with those with other morphologies, such as nano-octahedra, nanocubes, and nanorods.[34] In this study, under the same reaction conditions but varying Cr content and morphology, it is possible that the catalytic activity of sample nanoflakes ($Fe_{2.76}Cr_{0.24}O_4$) was greater than that of $Fe_{2.52}Cr_{0.48}O_4$ and $Fe_{2.24}Cr_{0.76}O_4$.

As reported previously, the removal of CBZ by freshwater microalga *Scenedesmus obliquus* and chlorine oxidation was quite poor, with half-lives of 4.41–5.20 d and 1.25 d, respectively.[11,12] In addition, CBZ was eliminated under UV 254 irradiation with a 10 W low-pressure mercury lamp.[12] The initial concentration of CBZ was 2 μmol L^{-1}, which was in accordance with the present study. The system of Liu *et al.*[12] required 20 min for 80% removal of CBZ. As shown in Fig. 3f, $Fe_{2.76}Cr_{0.24}O_4$ showed the fastest photocatalytic performance for the degradation of CBZ, with a removal rate of 80% at 5 min. The removal efficiency of CBZ in the present photocatalytic system was 4-fold higher than that of photodegradation. It is noteworthy that, under the optimum conditions (*i.e.*, 0.2 g L^{-1} $Fe_{2.52}Cr_{0.48}O_4$ 2.0 μmol L^{-1} CBZ, 1.0 mmol L^{-1} PMS, pH = 3.08), the removal percentage of total organic carbon for CBZ was found to be 71.1% after 40 min of reaction, and it increased to 76.4% at 60 min.

Extensive studies have demonstrated that magnetite and its doped compounds showed high catalytic activity, significant stability, and reusability in continuous cycle experiments, after limited cationic leaching.[34,49–51] Therefore, after completion of the degradation reaction, the dissolved Fe and Cr concentrations were less than 0.60 mg L^{-1} and 0.23 mg L^{-1}, respectively, accounting for about <0.10 wt% of Fe and <0.23 wt% of Cr content in the added solid catalyst, demonstrating good stability and reusability.

3.5. Major active species and reaction mechanism

In order to investigate the major active species during the degradation of CBZ in $Fe_{3-x}Cr_xO_4$/UV/PMS systems, scavenger agents were added to quench the reactive oxygen species (ROS). *Tert*-butyl alcohol (*t*-BuOH) and *p*-benzoquinone were used to quench $^{\bullet}OH$ and $O_2^{\bullet-}$, respectively, while ethanol (EtOH) was used to quench $^{\bullet}OH$ and $SO_4^{\bullet-}$ concurrently. As shown in Fig. 4, in the system containing *p*-benzoquinone, the degradation of CBZ was completed within 30 min, which was comparable to the system without quenching agents. The results demonstrated a negligible role of $O_2^{\bullet-}$ in the degradation. In contrast, the addition of *t*-BuOH led to a sharp decrease in the degradation efficiency of CBZ, with only 46.6% CBZ degraded due to the quenching of $^{\bullet}OH$. After EtOH addition, the quenching of $^{\bullet}OH$ and $SO_4^{\bullet-}$ simultaneously decreased the degradation of CBZ by more than 91%. Obviously, $^{\bullet}OH$ and $SO_4^{\bullet-}$ radicals coexisted in the reaction system, and together contributed to the oxidative degradation of CBZ. Studies have shown that $^{\bullet}OH$ radicals were generated by the reaction between $SO_4^{\bullet-}$ radicals and H_2O/OH^-, which ultimately resulted in the coexistence of $^{\bullet}OH$ and $SO_4^{\bullet-}$ radicals. The main reaction mechanisms include eqn (2), (4) and (9):[42–44]

$$SO_4^{\bullet-} + H_2O \rightarrow {}^{\bullet}OH + SO_4^{2-} + H^+ \quad (9)$$

In addition, ESR tests with DMPO (5,5-dimethyl-1-pyrroline *N*-oxide) spin-trapping were conducted to identify the $^{\bullet}OH$ and $SO_4^{\bullet-}$ radicals generated (Fig. 5). These two radicals were detected based on the signals of DMPO–$^{\bullet}OH$ and DMPO–$SO_4^{\bullet-}$ adducts. With only PMS, no signal was detected under dark conditions, and clear ESR four-line patterns assigned to DMPO–$^{\bullet}OH$ adducts, *i.e.*, characteristic signals of 1 : 2 : 2 : 1 quartet with hyperfine splitting constants: $\alpha_H = \alpha_N = 14.8$ G, gradually evolved under UV light irradiation. Almost no DMPO–$SO_4^{\bullet-}$ signal was detected in the reaction system. After utilizing $Fe_{2.52}Cr_{0.48}O_4$ as an activator, the DMPO–$^{\bullet}OH$ signals were sharply increased at different time intervals, and DMPO–$SO_4^{\bullet-}$ signals were detected along with $^{\bullet}OH$, suggesting the formation of both radical species. Studies suggest that the low-intensity signal associated with DMPO–$SO_4^{\bullet-}$ adducts is usually accompanied by the signal from DMPO–$^{\bullet}OH$ adducts.[52] This behaviour was possibly attributed to the fast transformation from $SO_4^{\bullet-}$ to $^{\bullet}OH$ *via* nucleophilic substitution by H_2O/OH^- as depicted in eqn (4) and (9).

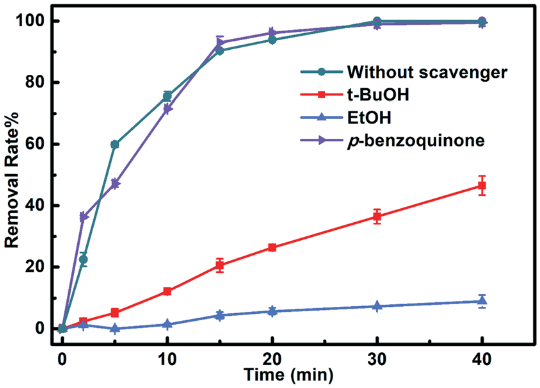

Fig. 4 Degradation of CBZ in the $Fe_{3-x}Cr_xO_4$/UV/PMS system with and without scavenging agents namely *t*-BuOH, EtOH, and *p*-benzoquinone.

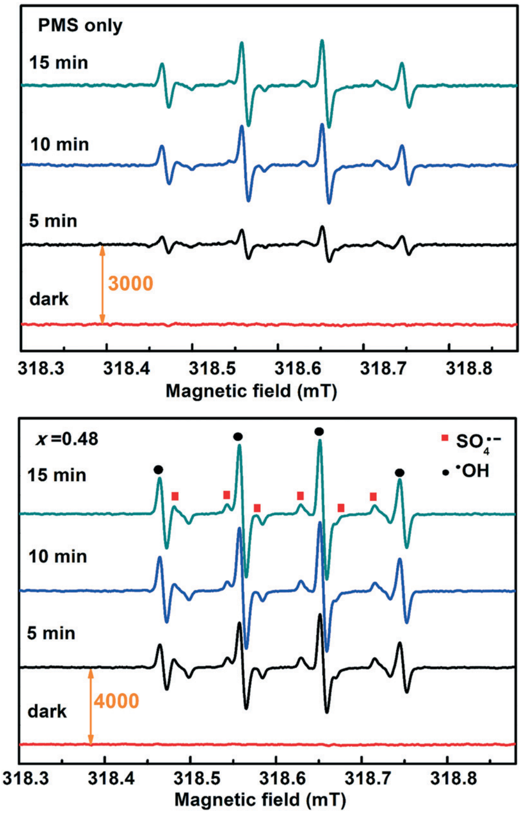

Fig. 5 ESR spin trapping of OH and $SO_4^{\bullet-}$ in aqueous solution with DMPO in systems containing PMS alone and PMS/$Fe_{2.52}Cr_{0.48}O_4$ under UVA irradiation.

3.6. Assessment of 4-chlorophenol formation

According to the chemical structure, CBZ contains a 4-chlorophenyl functional group suggesting that the degradation of CBZ leads to the formation of 4-chlorophenol (4-CP) in the presence of $^{\bullet}OH$ and $SO_4^{\bullet-}$ radicals. 4-CP is an intermediate product generated by the $Fe_{2.52}Cr_{0.48}O_4$/UV/PMS catalytic degradation of CBZ. It was identified by GC-MS in a full scan mode. Compared with the blank samples, only a single peak was observed at the retention time of 12.3 min in the treated samples. Based on the NIST mass spectral database and the retention time/mass spectrum of the 4-CP standard, the observed peak was assigned to 4-CP (Fig. 6). The molecular ion peak was detected at *m*/*z* 200.1, with the corresponding structure of (4-chlorophenoxy)(trimethyl)silane (4-CP-TMS), which was generated *via* the reaction between 4-CP and BSTFA. The fragments of *m*/*z* 185.1, 157.1, and 111.0 were assigned to the structures lacking the single methyl group, three methyl groups, and one silyloxy group in 4-CP-TMS, respectively. Their isotopic peaks at *m*/*z* 187.1, 159.1, and 113.0 were also observed, with an isotopic abundance ratio of approximately 3 : 1, indicating the presence of a single chlorine atom in the intermediate product. A previous study demonstrated the production of 4-CP during the UV photolysis of CBZ; however, 4-CP was not quantified during the degradation process.[13] We also attempted to identify other potential intermediates *via* UHPLC-HRMS. Several intermediates of CBZ, which lacked chlorophenyl, pivaldehyde, or chlorine, were identified during direct

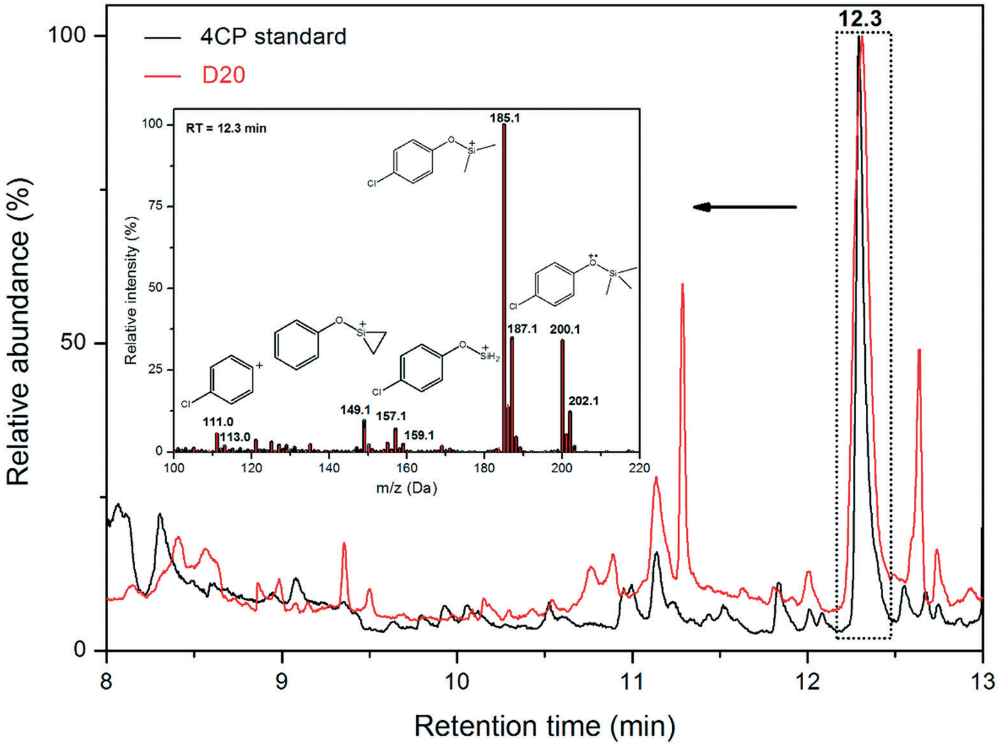

Fig. 6 Total ion chromatogram of the sample D20 and the 4-CP standard *via* GC-MS analysis; inset, the mass spectrum of D20 and 4-CP standards at a retention time of 12.3 min.

photolysis,[12,13] but not in the present study (Fig. S2–S4†). The loss of products with high molecular weight can be explained by the stronger oxidation/reduction capacity under photocatalysis, which leads to advanced degradation of CBZ and formation of small molecular products such as 4-CP.

The concentrations of 4-CP at reaction intervals of 0, 10 min, 20 min, and 40 min were detected by GC-MS in the selected ion monitoring (SIM) mode (Fig. S5† and Table 4). No 4-CP was found before the start of the degradation reaction. With increasing reaction time, the concentration of 4-CP was raised to 1.94×10^{-4} μmol L^{-1} at 10 min and peaked at 6.65×10^{-1} μmol L^{-1} at 20 min. The maximum transformation rate of 4-CP from CBZ was increased to 33.3%, suggesting that the oxygen atom located in the 4-chlorophenoxy group of CBZ was an active interaction site that was easily attacked by $^{\bullet}OH$ and $SO_4^{\bullet-}$ radicals. At the reaction time of 40 min, the 4-CP level was decreased to 1.33×10^{-1} μmol L^{-1}, which was basically equal to 20% of 4-CP abundance at 20 min. These findings explain the stoichiometric relationship between CBZ and 4-CP. In addition, Descorme[53] reported that photocatalysis was an effective way for the removal of chlorophenols, suggesting that 4-CP was further decomposed in the $Fe_{2.52}Cr_{0.48}O_4$/UV/PMS catalytic system and completely eliminated at an adequate reaction time.

It is well known that chlorophenols are toxic pollutants. Due to their toxicity to aquatic organisms, a number of official regulatory organizations have set standards stipulating the maximum environmental concentrations for chlorophenols.[15,16] Since 4-CP is one of the primary chlorophenols, ecological risks posed by 4-CP during CBZ degradation should be assessed using the risk quotient approach.[23] Based on sufficient toxicity data (Table S2†) collected from the ECOTOX knowledgebase,[14] the PNECs of 4-CP were derived using statistical extrapolation techniques. Fig. 7 shows the species sensitivity distribution (SSD) profiles of 4-CP including chronic and acute toxicity. Correlation coefficients ($R^2 > 0.98$) and significant levels ($p < 0.01$) reveal goodness of fit for the SSD curves. The calculated PNECs of 4-CP were 0.28 mg L^{-1} for chronic effects and 1.86 mg L^{-1} for acute effects. As shown in Fig. 7, the yields of 4-CP during the CBZ degradation process were lower than both the PNEC values (HC_5 = 0.28 mg L^{-1} for chromic toxicity and HC_5 = 1.86 mg L^{-1} for acute toxicity), indicating the absence of high risks posed by 4-CP in this study. However, the risk quotient of 4-CP is changed under experimental conditions such as the initial concentrations of CBZ. Thus, the degradation intermediates during photocatalysis of environmental pollutants need to be monitored, especially those containing chemical structures of highly toxic small molecules such as chlorophenols and nitrophenols.[15,54] In order to prevent secondary contamination due to catalytic degradation of the target pollutants, the transformation rates and ecological risk of product intermediates should be assessed using a standard-based quantification.

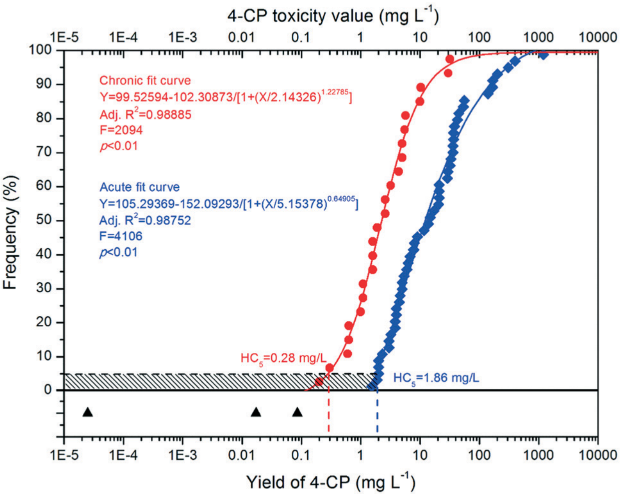

Fig. 7 Species sensitivity distribution curves of climbazole showing acute and chronic effects, and box plots representing the measured concentrations of climbazole in surface water and effluents. ● represents chronic effects, and ■ represents acute effects. The shadow zone indicates the expected safety of 95% of species in the aquatic environment. ▲ represents the detected yield of 4-CP during CBZ degradation at 10–40 min.

4. Conclusions

In this study, a new floral array of chromium-substituted magnetite nanoparticles was synthesized *via* microwave-assisted synthesis. The results revealed that the isomorphous replacement of Cr greatly influenced the magnetite morphology, micro-structure and photocatalytic activity. Under optimized reaction conditions, the removal efficiency of CBZ was at least four-fold higher than that of photodegradation, biodegradation, or chlorination reported by other studies. The improved catalytic activity of magnetite may be attributed to Cr ions directly participating in activation of PMS. Based on the indirect (quenching agents) and direct

Table 4 Concentrations, transformation rates and risk quotients of 4-CP at different times by degradation of CBZ

Reaction time (min)	C_{4CP} (μmol L^{-1})	Transformation rate (%)[a]	C_{4CP} (mg L^{-1})	Chronic RQ	Acute RQ
0	0	0	0	0	0
10	1.94×10^{-4}	9.70×10^{-4}	2.50×10^{-7}	8.92×10^{-7}	1.34×10^{-7}
20	6.65×10^{-1}	33.3	8.55×10^{-2}	3.05×10^{-1}	4.60×10^{-2}
40	1.33×10^{-1}	6.67	1.72×10^{-2}	6.14×10^{-2}	9.25×10^{-3}

[a] The initial concentration of CBZ (C_0) is 2 μmol L^{-1}, then the transformation rate is equal to ($C_{4\text{-}CP}/C_0 \times 100\%$).

(DMPO spin-trapping ESR) approaches, $^{\bullet}OH$ and $SO_4^{\bullet-}$ radicals were detected as the dominant reactive oxygen species in the $Fe_{2.52}Cr_{0.48}O_4$/UVA/PMS system, which facilitated the transformation of CBZ. 4-CP was identified as a primary reaction intermediate in the CBZ transformation and was not associated with any elevated risks for aquatic organisms.

Consequently, our results have implications for environmental remediation in terms of (1) broad prospects of the UV/Cr-magnetite/PMS technique with excellent removal efficiency, (2) good reusability of environmentally-friendly Cr-magnetite, and (3) decrease of risks from highly toxic emerging contaminants to low toxicity intermediates.

Conflicts of interest

There are no conflicts to declare.

Acknowledgements

We gratefully acknowledge the financial support from the Natural Science Foundation of China (No. 41602031 and 21507163) and the China Postdoctoral Science Foundation Funded Project (No. 2016 M592464).

References

1 U. Bernauer, L. Bodin, L. Celleno, Q. Chaudhry, P. J. Coenraads, M. Dusinska, J. Ezendam, E. Gaffet, C. L. Galli and B. Granum, *SCCS Addendum to the Opinion on Climbazole (P64) ref. SCCS/1506/13*, Ed. Publications Office of the European Union, Luxembourg, 2018.

2 SCCP. Opinion on climbazole. 2009, [cited 2017 Jan. 21st]; Available from: http://ec.europa.eu/health/archive/ph_risk/committees/04_sccp/docs/sccp_o_164.pdf.

3 Q. Q. Zhang, G. G. Ying, Z. F. Chen, Y. S. Liu, W. R. Liu and J. L. Zhao, Multimedia fate modeling and risk assessment of a commonly used azole fungicide climbazole at the river basin scale in China, *Sci. Total Environ.*, 2015, **520**, 39–48.

4 ECHA. Justification for the selection of a candidate CoRAP substance (climbazole). 2013.

5 Z. F. Chen and G. G. Ying, Occurrence, fate and ecological risk of five typical azole fungicides as therapeutic and personal care products in the environment: A review, *Environ. Int.*, 2015, **84**, 142–153.

6 W. R. Liu, Y. Y. Yang, Y. S. Liu, L. J. Zhang, J. L. Zhao, Q. Q. Zhang, M. Zhang, J. N. Zhang, Y. X. Jiang and G. G. Ying, Biocides in wastewater treatment plants: Mass balance analysis and pollution load estimation, *J. Hazard. Mater.*, 2017, **329**, 310–320.

7 E. Richter, A. Wick, T. A. Ternes and A. Coors, Ecotoxicity of climbazole, a fungicide contained in anti-dandruff shampoo, *Environ. Toxicol. Chem.*, 2013, **32**, 2816–2825.

8 M. Kahle, I. J. Buerge, A. Hauser, M. D. Muller and T. Poiger, Azole fungicides: Occurrence and fate in wastewater and surface waters, *Environ. Sci. Technol.*, 2008, **42**, 7193–7200.

9 A. Pacholak, J. Simlat, A. Zgola-Grzeskowiak and E. Kaczorek, Biodegradation of clotrimazole and modification of cell properties after metabolic stress and upon addition of saponins, *Ecotoxicol. Environ. Saf.*, 2018, **161**, 676–682.

10 A. Rosch, S. Anliker and J. Hollender, How biotransformation influences toxicokinetics of azole fungicides in the aquatic invertebrate *Gammarus pulex*, *Environ. Sci. Technol.*, 2016, **50**, 7175–7188.

11 C. G. Pan, F. J. Peng and G. G. Ying, Removal, biotransformation and toxicity variations of climbazole by freshwater algae *Scenedesmus obliquus*, *Environ. Pollut.*, 2018, **240**, 534–540.

12 W. R. Liu, G. G. Ying, J. L. Zhao, Y. S. Liu, L. X. Hu, L. Yao, Y. Q. Liang and F. Tian, Photodegradation of the azole fungicide climbazole by ultraviolet irradiation under different conditions: Kinetics, mechanism and toxicity evaluation, *J. Hazard. Mater.*, 2016, **318**, 794–801.

13 G. Castro, J. Casado, I. Rodriguez, M. Ramil, A. Ferradas and R. Cela, Time-of-flight mass spectrometry assessment of fluconazole and climbazole UV and UV/H_2O_2 degradability: Kinetics study and transformation products elucidation, *Water Res.*, 2016, **88**, 681–690.

14 USEPA, *The ECOTOX Knowledgebase*, 2019, Available from: https://cfpub.epa.gov/ecotox/.

15 U. G. Ahlborg and T. M. Thunberg, Chlorinated phenols: Occurrence, toxicity, metabolism, and environmental impact, *Crit. Rev. Toxicol.*, 1980, **7**, 1–35.

16 A. O. Olaniran and E. O. Igbinosa, Chlorophenols and other related derivatives of environmental concern: Properties, distribution and microbial degradation processes, *Chemosphere*, 2011, **83**, 1297–1306.

17 Y. H. Zhong, X. L. Liang, Z. S. He, W. Tan, J. X. Zhu, P. Yuan, R. L. Zhu and H. P. He, The constraints of transition metal substitutions (Ti, Cr, Mn, Co and Ni) in magnetite on its catalytic activity in heterogeneous Fenton and UV/Fenton reaction: From the perspective of hydroxyl radical generation, *Appl. Catal., B*, 2014, **150–151**, 612–618.

18 P. Chen, F. Wang, Z.-F. Chen, Q. Zhang, Y. Su, L. Shen, K. Yao, Y. Liu, Z. Cai, W. Lv and G. Liu, Study on the photocatalytic mechanism and detoxicity of gemfibrozil by a sunlight-driven TiO_2/carbon dots photocatalyst: The significant roles of reactive oxygen species, *Appl. Catal., A*, 2017, **204**, 250–259.

19 Q. Zhang, W. Zhou, Y. Cui, C. Lyu, T. Liu, R. Zhang, R. Zhang, J. Zheng, Z. Shi, C. Lu and L. Guo, Iron triad nanomaterials and their sustainable application in the environment, *Environ. Sci.: Nano*, 2018, **5**, 246–256.

20 S. J. Yang, H. P. He, D. Q. Wu, D. Chen, X. L. Liang, Z. H. Qin, M. D. Fan, J. X. Zhu and P. Yuan, Decolorization of methylene blue by heterogeneous Fenton reaction using $Fe_{3-x}Ti_xO_4$ ($0 \leqq x \leqq 0.78$) at neutral pH values, *Appl. Catal., B*, 2009, **89**, 527–535.

21 M. D. Sampson, J. D. Froehlich, J. M. Smieja, E. E. Benson, I. D. Sharp and C. P. Kubiak, Direct observation of the reduction of carbon dioxide by rhenium bipyridine catalysts, *Energy Environ. Sci.*, 2013, **6**, 3748.

22 G. Wei, X. Liang, Z. He, Y. Liao, Z. Xie, P. Liu, S. Ji, H. He, D. Li and J. Zhang, Heterogeneous activation of Oxone by

substituted magnetites $Fe_{3-x}M_xO_4$ (Cr, Mn, Co, Ni) for degradation of Acid Orange II at neutral pH, *J. Mol. Catal. A: Chem.*, 2015, **398**, 86–94.

23 J. De Bruijn, B. G. Hansen, S. Johansson, M. Luotamo, S. J. Munn, C. Musset, S. I. Olsen, H. Olsson, A. B. Paya-Perez, F. Pedersen, K. Rasmussen and B. Sokull-Kluttgen, *Technical guidance document on risk assessment Part II*, 2003, [cited 2017 Sep 18th]; Available from: http://publications.jrc.ec.europa.eu/repository/handle/JRC23785.

24 M. D. Hernando, M. Mezcua, A. R. Fernández-Alba and D. Barceló, Environmental risk assessment of pharmaceutical residues in wastewater effluents, surface waters and sediments, *Talanta*, 2006, **69**, 334–342.

25 U. Schwertmann, The influence of aluminum on iron oxides. Part II. Preparation and properties of Al-substituted hematites, *Clays Clay Miner.*, 1979, **27**, 105–112.

26 W. Li, X. Liang, P. An, X. Feng, W. Tan, G. Qiu, H. Yin and F. Liu, Mechanisms on the morphology variation of hematite crystals by Al substitution: The modification of Fe and O reticular densities, *Sci. Rep.*, 2016, **6**, 35960.

27 M. A. Wells, R. W. Fitzpatrick, R. J. Gilkes and J. Dobson, Magnetic properties of metal-substituted haematite, *Geophys. J. Int.*, 1999, **138**, 571–580.

28 S. J. Gregg and K. S. W. Sing, *Adsorption, Surface Area and Porosity. 2nd edn*, Academic Press, London, 1982.

29 S. Brunauer, L. S. Deming, W. E. Deming and E. Teller, On a theory of the van der Waals adsorption of gases, *J. Am. Chem. Soc.*, 1940, **62**, 1723–1732.

30 Y.-C. Chiang, P.-C. Chiang and C.-P. Huang, Effects of pore structure and temperature on VOC adsorption on activated carbon, *Carbon*, 2001, **39**, 523–534.

31 J. C. Groen, L. A. Peffer and J. Pérez-Ramírez, Pore size determination in modified micro-and mesoporous materials. Pitfalls and limitations in gas adsorption data analysis, *Microporous Mesoporous Mater.*, 2003, **60**, 1–17.

32 A. Y. Khodakov, A. Griboval-Constant, R. Bechara and V. L. Zholobenko, Pore size effects in Fischer Tropsch synthesis over cobalt-supported mesoporous silicas, *J. Catal.*, 2002, **206**, 230–241.

33 S. Tiwari, R. Prakash, R. Choudhary and D. Phase, Oriented growth of Fe_3O_4 thin film on crystalline and amorphous substrates by pulsed laser deposition, *J. Phys. D: Appl. Phys.*, 2007, **40**, 4943.

34 Y. H. Zhong, L. Yu, Z.-F. Chen, H. P. He, F. Ye, G. Cheng and Q. X. Zhang, Microwave-assisted synthesis of Fe_3O_4 nanocrystals with predominantly exposed facets and their heterogeneous UVA/Fenton catalytic activity, *ACS Appl. Mater. Interfaces*, 2017, **9**, 29203–29212.

35 S. A. Chambers, T. C. Droubay, T. C. Kaspar, I. H. Nayyar, M. E. McBriarty, S. M. Heald, D. J. Keavney, M. E. Bowden and P. V. Sushko, Electronic and Optical Properties of a Semiconducting Spinel (Fe_2CrO_4), *Adv. Funct. Mater.*, 2017, **27**, 1605040.

36 T. Scott, G. Allen, P. Heard and M. Randell, Reduction of U(VI) to U(IV) on the surface of magnetite, *Geochim. Cosmochim. Acta*, 2005, **69**, 5639–5646.

37 X. Liang, Y. Zhong, W. Tan, J. Zhu, P. Yuan, H. He and Z. Jiang, The influence of substituting metals (Ti, V, Cr, Mn, Co and Ni) on the thermal stability of magnetite, *J. Therm. Anal. Calorim.*, 2012, **111**, 1317–1324.

38 V. Chandra, J. Park, Y. Chun, J. W. Lee, I.-C. Hwang and K. S. Kim, Water-dispersible magnetite-reduced graphene oxide composites for arsenic removal, *ACS Nano*, 2010, **4**, 3979–3986.

39 O. N. Shebanova and P. Lazor, Raman spectroscopic study of magnetite ($FeFe_2O_4$): a new assignment for the vibrational spectrum, *J. Solid State Chem.*, 2003, **174**, 424–430.

40 O. N. Shebanova and P. Lazor, Raman study of magnetite (Fe_3O_4): laser-induced thermal effects and oxidation, *J. Raman Spectrosc.*, 2003, **34**, 845–852.

41 I. Chamritski and G. Burns, Infrared-and Raman-active phonons of magnetite, maghemite, and hematite: a computer simulation and spectroscopic study, *J. Phys. Chem. B*, 2005, **109**, 4965–4968.

42 G. P. Anipsitakis and D. D. Dionysiou, Radical generation by the interaction of transition metals with common oxidants, *Environ. Sci. Technol.*, 2004, **38**, 3705–3712.

43 E. Hayon, A. Treinin and J. Wilf, Electronic spectra, photochemistry, and autoxidation mechanism of the sulfite-bisulfite-pyrosulfite systems. SO_2^-, SO_3^-, SO_4^-, and SO_5^- radicals, *J. Am. Chem. Soc.*, 1972, **94**, 47–57.

44 H. Liu, T. A. Bruton, W. Li, J. V. Buren, C. Prasse, F. M. Doyle and D. L. Sedlak, Oxidation of benzene by persulfate in the presence of Fe(III)- and Mn(IV)-containing oxides: Stoichiometric efficiency and transformation products, *Environ. Sci. Technol.*, 2016, **50**, 890–898.

45 C. Couteau, M. Jadaud, F. Peigne and L. J. M. Coiffard, Influence of pH on the photodegradation kinetics under UV light of climbazole solutions, *Analusis*, 2000, **28**, 557–560.

46 N. S. Shah, X. He, J. A. Khan, H. M. Khan, D. L. Boccelli and D. D. Dionysiou, Comparative studies of various iron-mediated oxidative systems for the photochemical degradation of endosulfan in aqueous solution, *J. Photochem. Photobiol., A*, 2015, **306**, 80–86.

47 F. Magalhães, M. Pereira, S. Botrel, J. Fabris, W. Macedo, R. Mendonca, R. Lago and L. Oliveira, Cr-containing magnetites $Fe_{3-x}Cr_xO_4$: The role of Cr^{3+} and Fe^{2+} on the stability and reactivity towards H_2O_2 reactions, *Appl. Catal., A*, 2007, **332**, 115–123.

48 H. Sun and S. Wang, *Chapter 6: Catalytic oxidation of organic pollutants in aqueous solution using sulfate radicals, in Catalysis: Volume 27*, The Royal Society of Chemistry, 2015, pp. 209–247.

49 Y. H. Zhong, X. L. Liang, Y. Zhong, J. X. Zhu, S. Y. Zhu, P. Yuan, H. P. He and J. Zhang, Heterogeneous UV/Fenton degradation of TBBPA catalyzed by titanomagnetite: catalyst characterization, performance and degradation products, *Water Res.*, 2012, **46**, 4633–4644.

50 Y. H. Zhong, X. L. Liang, W. Tan, Y. Zhong, H. P. He, J. X. Zhu, P. Yuan and Z. Jiang, A comparative study about the effects of isomorphous substitution of transition metals (Ti, Cr, Mn, Co and Ni) on the UV/

Fenton catalytic activity of magnetite, *J. Mol. Catal. A: Chem.*, 2013, **372**, 29–34.

51 M. Munoz, Z. M. de Pedro, J. A. Casas and J. J. Rodriguez, Preparation of magnetite-based catalysts and their application in heterogeneous Fenton oxidation: A review, *Appl. Catal., A*, 2015, **176–177**, 249–265.

52 Y. Zhou, X. Wang, C. Zhu, D. D. Dionysiou, G. Zhao, G. Fang and D. Zhou, New insight into the mechanism of peroxymonosulfate activation by sulfur-containing minerals: Role of sulfur conversion in sulfate radical generation, *Water Res.*, 2018, **142**, 208–216.

53 C. Descorme, Catalytic wastewater treatment: Oxidation and reduction processes. Recent studies on chlorophenols, *Catal. Today*, 2017, **297**, 324–334.

54 R. O. Beauchamp, Jr., R. D. Irons, D. E. Rickert, D. B. Couch and T. E. Hamm, Jr., A critical review of the literature on nitrobenzene toxicity, *Crit. Rev. Toxicol.*, 1982, **11**, 33–84.